

Supercontinuum generation in Rubidium vapour

Rezzak Ali¹, Buru Kakum ^{1*}, Rickey Marngar¹ and Rohit Mukherjee², Nitu Borgohain¹

¹ Department of Physics, University of Science and Technology Meghalaya, India-793101

²Theoretical Photonics Group, Department of Physics, Sarala Birla University, Jharkhand, India-835103

*E-mail: burukakum2020@gmail.com

Abstract: We present a theoretical study of supercontinuum generation in a Rubidium vapor cell under the conditions of electromagnetically induced transparency (EIT). A weak probe pulse and a strong control laser beam were utilized within a lambda-type excitation scheme. We identified a significant Kerr nonlinearity on the order of $10^3 \text{ W}^{-1}\text{m}^{-1}$ and low group velocity dispersion on the order of $10^{-20} \text{ s}^2\text{m}^{-1}$ in the Rubidium vapor cell of length 2.54 cm at a probe wavelength of 781 nm. These parameters facilitated the generation of a 35nm supercontinuum, characterized by pronounced oscillations resulting from self-phase modulation and optical wave breaking. The findings suggest potential applications in nonlinear optical devices and spectroscopy.

Keywords: Electromagnetically induced transparency, supercontinuum generation, Kerr nonlinearity, dispersions, linear and nonlinear susceptibilities.

1. Introduction

The optical supercontinuum (SC) emerges when high-power narrowband optical pulses propagate through a nonlinear medium, resulting in a broad spectrum. This broadening phenomenon is attributed to several nonlinear processes[1-8]. These phenomena hinge significantly on two key properties of the optical medium: its optical nonlinearity strength and its low dispersion profile. A low dispersion profile not only decreases the power demand but also improves the quality of the produced SC [6-9]. Although SC generation has been demonstrated in various nonlinear media, the majority of experimental and theoretical investigations have concentrated on optical fibers and photonic crystal fibers (PCFs). This focus persists because these mediums allow for the engineering of effective nonlinearity and the tailored manipulation of chromatic dispersion to desired specifications [8-10].

When considering the interaction of light with atomic systems, especially within atomic vapours like Rubidium (Rb), numerous advantages over PCFs become apparent [11-14]. Atomic vapours showcase remarkable Kerr nonlinearities stemming from robust resonant interactions, enabling substantial nonlinear effects at notably lower power levels and with reduced absorption. In atomic systems, tuneable parameters such as laser detuning and intensity can be meticulously regulated, facilitating dynamic adjustments to nonlinear optical properties. Additionally, at specific resonant wavelengths, atomic vapours demonstrate minimal absorption, enhancing their efficiency for nonlinear processes.



Recent years have witnessed substantial research efforts directed towards enhancing nonlinear susceptibilities in atomic media, particularly focusing on Rubidium (Rb) atoms [15-17]. Theoretical and experimental investigations concerning Rb aim to achieve significant nonlinear susceptibilities while minimizing linear absorption, often leveraging electromagnetically induced transparency (EIT). EIT, capable of manipulating light's group velocity, has garnered attention for its potential applications in optoelectronics and quantum information science, particularly in atomic media [18, 19]. The interplay of EIT and slow optical pulse propagation in atomic systems has sparked significant interest due to its potential applications in optoelectronics and quantum information science. The role of Kerr nonlinearity in determining the characteristics of optical solitons, four-wave mixing, and all-optical switching in atomic vapors has been extensively explored [20, 21]. In the realm of EIT, soliton generation has been a focal point due to the unique attributes of Rb atomic systems. Recent studies, such as that by Han *et al.* [22], have showcased the generation of optical solitons in Rb vapor cells using EIT in a three-level Λ -type configuration, enhancing Kerr nonlinearity and reducing group velocity. Additionally, research by Zhang *et al.* [23], delved into third-order dispersion and self-steepening, leading to the formation of higher-order solitons. Pioneering work by Xiao *et al.* [24], reported bistable behaviour in an EIT medium comprising Rb atoms, emphasizing the potential of EIT-induced bistability for optical memory elements and switches. Further advancements by Chen *et al.* [25], explored the influence of atomic coherence on bistability, offering new avenues for tunability in photonic devices. Thus, this article aims to demonstrate the presence of substantial Kerr nonlinearity within the transparency window of Rb vapor and to exploit it for supercontinuum generation in the system.

The structure of the article is outlined below: 2nd section elaborates the mathematical model as well as equations. 3rd section presents the results along with corresponding discussions. Finally, the conclusion of our work is provided in Section 4.

2. Mathematical Model and Equations

In this study, the system considered is a rubidium vapour having three energy levels [26], as shown in figure 1. A faint probe pulse with angular frequency ω_p in the transition ($5S_{1/2} \rightarrow 5P_{3/2}$) and a potent control laser beam with angular frequency ω_c in the transition ($5P_{3/2} \rightarrow 5D_{5/2}$) are utilized in a cascade-type configuration. This configuration is suitable for achieving EIT in the system. We represent the states $5S_{1/2}$, $5P_{3/2}$, and $5D_{5/2}$, as $|1\rangle$, $|2\rangle$ and $|3\rangle$, respectively, for simplicity.

The total Hamiltonian of the system is expressed as,

$$H = \hbar\omega_1|1\rangle\langle 1| + \hbar\omega_2|2\rangle\langle 2| + \hbar\omega_3|3\rangle\langle 3| - \hbar\Omega_p e^{-i\omega_p t}|2\rangle\langle 1| - \hbar\Omega_c|3\rangle\langle 2| - \hbar\Omega_p e^{i\omega_p t}|1\rangle\langle 2| - \hbar\Omega_c e^{i\omega_c t}|2\rangle\langle 3|, \quad (1)$$

where Ω_p and Ω_c are probe and control Rabi frequencies, defined as $\Omega_p = \frac{\mu_{21}\epsilon_c}{\hbar}$ and $\Omega_c = \frac{\mu_{32}\epsilon_c}{\hbar}$, respectively, with μ_{21} and μ_{32} are being the dipole moments of the probe and control laser transitions.

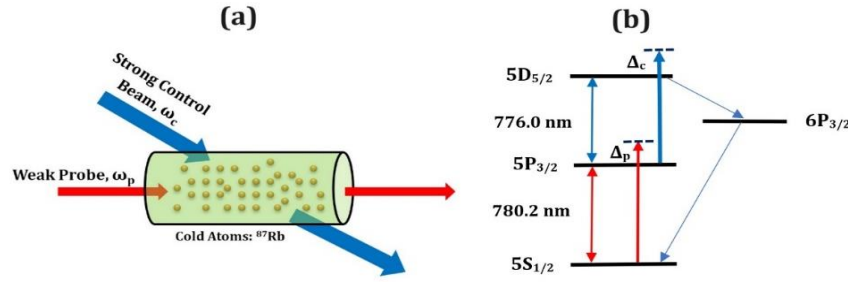


Figure 1: (a) Schematic of the rubidium cell with probe and control field interaction, (b) Energy level diagram with ladder-type excitation scheme of the rubidium vapour system.

The equations of motion, utilizing the density matrix approximation, are as follows:

$$\frac{d}{dt} \tilde{\rho}_{21} = i \left(\Delta_p + i \frac{\gamma_{21}}{2} \right) \tilde{\rho}_{21} + i \Omega_p (\tilde{\rho}_{11} - \tilde{\rho}_{22}) + i \Omega_c^* \tilde{\rho}_{31}, \quad (2)$$

$$\frac{d}{dt} \tilde{\rho}_{32} = i \left(\Delta_c + i \frac{\gamma_{32}}{2} \right) \tilde{\rho}_{32} + i \Omega_c (\tilde{\rho}_{22} - \tilde{\rho}_{33}) + i \Omega_p^* \tilde{\rho}_{31}, \quad (3)$$

$$\frac{d}{dt} \tilde{\rho}_{31} = i (\Delta_p + \Delta_c + i \frac{\gamma_{31}}{2}) \tilde{\rho}_{31} + i \Omega_c \tilde{\rho}_{21} - i \Omega_p \tilde{\rho}_{32}, \quad (4)$$

where Δ_p and Δ_c represent the intersubband transition detunings, and γ_{21} , γ_{31} , and γ_{32} denotes the decay [26]. The susceptibility is divided into linear and nonlinear components, which is expressed by the given equation: $\chi_p = \chi^{(1)}(\omega_p) + \chi^{(3)}|E_p|^2$, here the investigation focuses on 3rd-order terms while higher orders are neglected. The susceptibilities is being represented as:

$$\chi^{(1)} = -\frac{N|\mu_{12}|^2}{\hbar\epsilon_0} \frac{D_p(0)}{D(0)}, \quad (5)$$

$$\chi^{(3)} = \frac{N|\mu_{12}|^4}{4\hbar^3\epsilon_0} \frac{(|\Omega_c|^2 + |D_p(0)|^2)D_p(0)}{|D(0)|^2 D(0)}, \quad (6)$$

where N is the carrier density, $D_p(0) = \Delta_p + \Delta_c + i \frac{\gamma_{31}}{2}$, and $D(0) = \left(\Delta_p + i \frac{\gamma_{21}}{2} \right) \left(\Delta_p + \Delta_c + i \frac{\gamma_{31}}{2} \right) - |\Omega_c|^2$.

Utilizing the conventional method outlined in [27], we can derive the propagation constant of the probe pulse as:

$$k(\omega) = \frac{\omega}{c} - \frac{\alpha D_p(\omega)}{D(\omega)}, \quad (7)$$

where, $\alpha = \frac{N\omega_p|\omega_{12}|^2}{2c\hbar\epsilon_0}$. The $K(\omega)$ is given in Taylor's series, concentrated with frequency of probe pulse ($\omega = 0$) given below:

$$K(\omega) = K(0) + K_1(0)\omega + \frac{1}{2}K_2(0)\omega^2 + \dots, \quad (8)$$

where $K_n(0)$ are given by $K_n(0) = \frac{d^n K}{d\omega^n} \Big|_{\omega=0}$. In physical terms, $K(0) = \phi + i\alpha/2$, where the Re and Im components represent the phase shift and absorption coefficient, respectively. Meanwhile, $K_1(0) = \frac{dK(\omega)}{d\omega} \Big|_{\omega=0}$ is related to the group velocity, expressed as $V_g = \text{Re} \left[\frac{1}{K'(0)} \right]$. The higher-order term $K_2(0) = \frac{d^2 K(\omega)}{d\omega^2} \Big|_{\omega=0}$ constitutes the GVD of probe pulse. It oversees alterations in the pulse shape during propagation and more loss/gain of the probe field intensity. $K_3(0) = \frac{d^3 K(\omega)}{d\omega^3} \Big|_{\omega=0}$ signifies the third-order dispersion (TOD), leading to increased spreading of the pulse in the temporal domain.

To investigate dynamics of pulse propagation, we consider the below NLSE for the $\tilde{\Omega}_p$:

$$i \frac{\partial \tilde{\Omega}_p}{\partial \xi} - \frac{1}{2} K_2(0) \frac{\partial^2 \tilde{\Omega}_p}{\partial T^2} + W |\tilde{\Omega}_p|^2 \tilde{\Omega}_p e^{-\alpha z} = 0 \quad (9)$$

where, $W = \alpha \left(\frac{|\Omega_c|^2 + |D_p(0)|^2}{|D(0)|^2} \right) \frac{D_p(0)}{D(0)}$. We choose the set of parameters of the atomic system in such a way that $\alpha \approx 0$; so that $e^{-\alpha z} = e^{-2\alpha z} = 1$. Introducing the retarded frame $z = \xi$ and $T = t - zK_1(0)$, and after suitable rescaling, the above equation can be recasted as:

$$i \frac{\partial A}{\partial \xi} - \frac{1}{2} \beta_2(0) \frac{\partial^2 A}{\partial T^2} - \frac{i}{6} \beta_3(0) \frac{\partial^3 A}{\partial T^3} + \gamma |A|^2 A = 0, \quad (10)$$

where $A = \frac{\hbar \left(\frac{cn\epsilon_0 S}{2} \right)^{\frac{1}{2}}}{\mu_{12}} \Omega_p$, $\gamma = W \left(\mu_{12} / \hbar \sqrt{\frac{cn\epsilon_0 S}{2}} \right)^2$; n represents the linear refractive index of the medium, while S denotes the cross-sectional area of the pump laser pulse. The provided equation is a modified form of the nonlinear Schrödinger equation, which has been derived to include second and third-order dispersions as well as Kerr nonlinearity. Equation (10) can be employed to investigate spectral broadening resulting from the combined effects of group velocity dispersion, third-order dispersion, and nonlinearity-induced self-phase modulation (SPM).

3. Results and Discussions

3.1 Linear and Nonlinear Susceptibilities

Prior to delving into the exploration of supercontinuum, it's important to delineate the notable characteristic of both linear as well as nonlinear susceptibilities under atomic system. The linear susceptibility primarily regulates pulse spreading and attenuation, whereas the nonlinear susceptibility is responsible for driving many nonlinear characteristics like SPM, XPM, and FWM, which play a crucial role in supercontinuum (SC) generation. In Figure 2, we illustrate the changes in the imaginary and real components of $\chi^{(1)}$ with respect to a normalized probe detuning Δ_p across various intensities of the control field Ω_c , utilizing equation (5). Here, the decay terms utilized are $\gamma_{21} = 6 \text{ MHz}$ and $\gamma_{31} = 0.97 \text{ MHz}$ [26]. The obtained values of $\chi^{(1)}$ are normalized with the term $\left(\frac{N|\mu_{12}|^2}{\hbar\epsilon_0} \right)$. Figure 2(a) demonstrates that when the first control field $\Omega_c = 0$ is absent, the probe field at resonance $\Delta_p = 0$ undergoes notable absorption, as indicated by a function of Gaussian-shaped peak at $\Delta_p = 0$. Whereas, when we introduce the control field, the

absorption peak breaks to two distinct peaks, creating this phenomenon known as electromagnetically induced transparency (EIT) window. The breadth of the EIT window widens as the strength of primary control field increases. In Figure 2(b), it is shown that without the strong control, the figure of $Re\chi^{(1)}$ displays a sharp decline around $\Delta_p = 0$. Upon introducing the strong control, the sharp decline transitions into an incline under EIT window, the magnitude of slope can be run by the control field. Consequently, adjusting the intensity of the primary control field effectively controls the group velocity of the probe field.

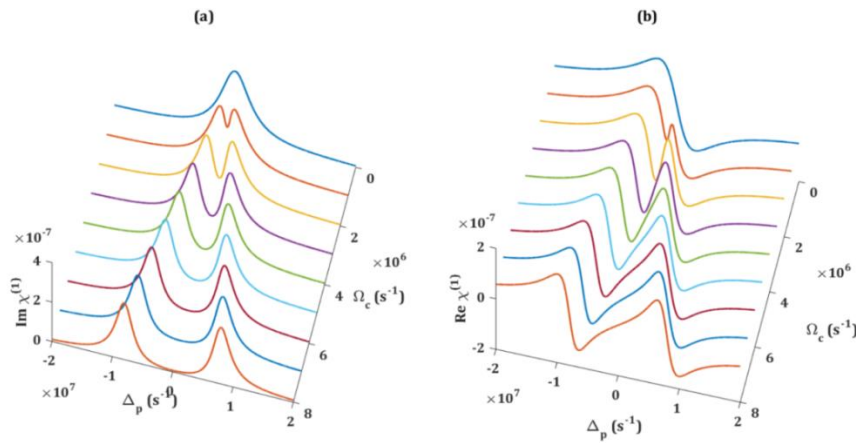


Figure 2: (a) The imaginary and (b) real components of $\chi^{(1)}$ are presented as functions of Δ_p for varying Rabi frequencies of the Ω_c . These $\chi^{(1)}$ values are normalized using $\left(\frac{N|\mu_{12}|^2}{\hbar\epsilon_0}\right)$.

To investigate the optical nonlinearity demonstrated by the atomic system, we present the change in $Re\chi^{(3)}$ as a function of Δ_p in Figure 3. Similarly, the values of $\chi^{(3)}$ obtained here are normalized using the term $\left(\frac{N|\mu_{12}|^4}{4\hbar^3\epsilon_0}\right)$. In Figure 3(a), the change is illustrated for various value under Ω_c while maintaining the detuning at ($\Delta_c = 0$). It's clear that when the control field is absent ($\Omega_c = 0$), $Re\chi^{(3)}$ exhibits a single peak positioned at $\Delta_p = 0$, coincidentally matching the location of the maximum of $Im(\chi^{(1)})$. Therefore, both the nonlinearity and absorption reach their peaks when $\Delta_p = 0$. With introduction of finite control fields which divides the incline of $Re(\chi^{(3)})$ into two peaks, and gap of two incline widens as the intensity of the control field increases. The impact of Δ_c on $Re\chi^{(3)}$ is observed in Figure 4(b). As detuning Δ_c increases from zero, the two peaks of $Re(\chi^{(3)})$ shift towards lower values of Δ_p , while they shift towards higher values of Δ_p when the control detuning decreases ($\Delta_c = 0$). These studies reveal that both the control Rabi frequency and detuning can adjusted to $Re(\chi^{(3)})$ values of any required probe frequency.

To investigate nonlinearity shown by atomic system, we depict the change in $Re\chi^{(3)}$ as a function of Δ_p in Figure 3. Likewise, the acquired $\chi^{(3)}$ values are normalized using the term $\left(\frac{N|\mu_{12}|^4}{4\hbar^3\epsilon_0}\right)$. In Figure 3(a), this change is shown for distinct values of Ω_c while keeping its detuning at ($\Delta_c = 0$). It's clear that when the control field is absent ($\Omega_c = 0$), $Re\chi^{(3)}$ displays a singular

peak at $\Delta_p = 0$, which happens to align with the peak of $Im(\chi^{(1)})$. As a result, both nonlinearity and absorption reach their peaks at $\Delta_p = 0$. When we introduce control field it divides the incline of $Re(\chi^{(3)})$ to two and the gap within both incline widens when intensity of control field increases. The impact of Δ_c on $Re\chi^{(3)}$ is investigated in Figure 4(b). When the detuning Δ_c increases from zero, the two peaks of $Re\chi^{(3)}$ shift towards lower values of Δ_p , whereas they shift towards higher values of Δ_p as the control detuning decreases from ($\Delta_c = 0$). These studies illustrate that both the control Rabi frequency and detuning have the capability to adjust values of $Re(\chi^{(3)})$ to required probe frequency.

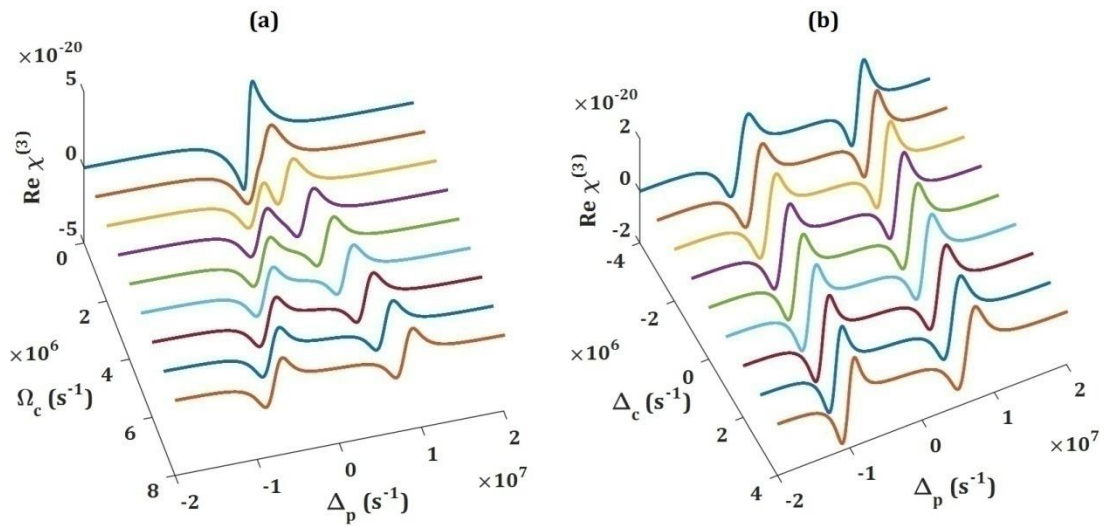


Figure 3 (a) The variation of $Re(\chi^{(3)})$ with Δ_p is depicted for different control field Rabi frequencies Ω_c along with their respective Δ_c . (b) Additionally, the $Re(\chi^{(3)})$ values are shown for various detunings of the control field Δ_c with respect to Δ_p . These values are normalized using $\left(\frac{N|\mu_{12}|^4}{4\hbar^3\epsilon_0}\right)$.

3.2 Supercontinuum generation

In this section, we utilize numerical simulation to investigate optical supercontinuum generation, taking advantage of the significant nonlinearity inherent in Rb vapor. To achieve supercontinuum generation at low power levels, it is crucial to select a probe pulse wavelength that experiences minimal absorption, low dispersion, and significant nonlinearity. Therefore, we opt for a probe detuning at $\Delta_p = 0.2 \times 10^7$ ps⁻¹, corresponding to a pump wavelength $\lambda_p = 781$ nm. At this probe detuning, without the application of the control field, absorption is notably high, with $Im\chi^{(1)} = 2.31 \times 10^{-7}$. However, when the control field is applied ($\Omega_c = 4 \times 10^6$ s⁻¹ with detuning $\Delta_c = 2 \times 10^6$ s⁻¹), absorption diminishes to $Im\chi^{(1)} = 0.14 \times 10^{-7}$, reduced by almost 17 times. This reduction is illustrated in Figure 4(a), where the vertical dotted line intersects the absorption profiles at the mentioned values. In our investigation, the Rb cell's length is 2.54 cm [3]. Given the short propagation distance and reduced absorption, attenuation

is neglected while studying SC generation. The values of higher-order dispersions and nonlinearity are as follows: $K_2 = -2.647 \times 10^{-19} \text{s}^2 \text{m}^{-1}$, $K_3 = -2.371 \times 10^{-25} \text{s}^3 \text{m}^{-1}$, $K_4 = 4.769 \times 10^{-31} \text{s}^4 \text{m}^{-1}$, $K_5 = 3.170 \times 10^{-36} \text{s}^5 \text{m}^{-1}$, $K_6 = 7.375 \times 10^{-42} \text{s}^6 \text{m}^{-1}$ and the nonlinear coefficient $\gamma = -5.74 \times 10^3 \text{W}^{-1} \text{m}^{-1}$. The dispersion parameter is $D = -\frac{2\pi c}{\lambda^2} K_2$, with its value at the pump wavelength λ_p being $D = 8.15 \times 10^5 \text{ps nm}^{-1} \text{m}^{-1}$. Figures 4(b) depict the group velocity dispersion profile K_2 with respect to probe detuning Δ_p , with the vertical dotted line indicating the detuning $\Delta_p = 0.2 \times 10^7 \text{ps}^{-1}$, intersecting the K_2 graph at its value $K_2 = 1.92 \times 10^{-21} \text{s}^2 \text{m}^{-1}$. In Figure 4(c), we plot the nonlinear coefficient γ versus Δ_p , with the vertical dotted line representing the probe detuning $\Delta_p = 0.2 \times 10^7 \text{ps}^{-1}$, intersecting the γ graph at its value $\gamma = -5.74 \times 10^3 \text{W}^{-1} \text{m}^{-1}$. These values of higher-order dispersions and the nonlinear coefficient are employed for the subsequent discussion on SC generation in Rb vapor in the following section.

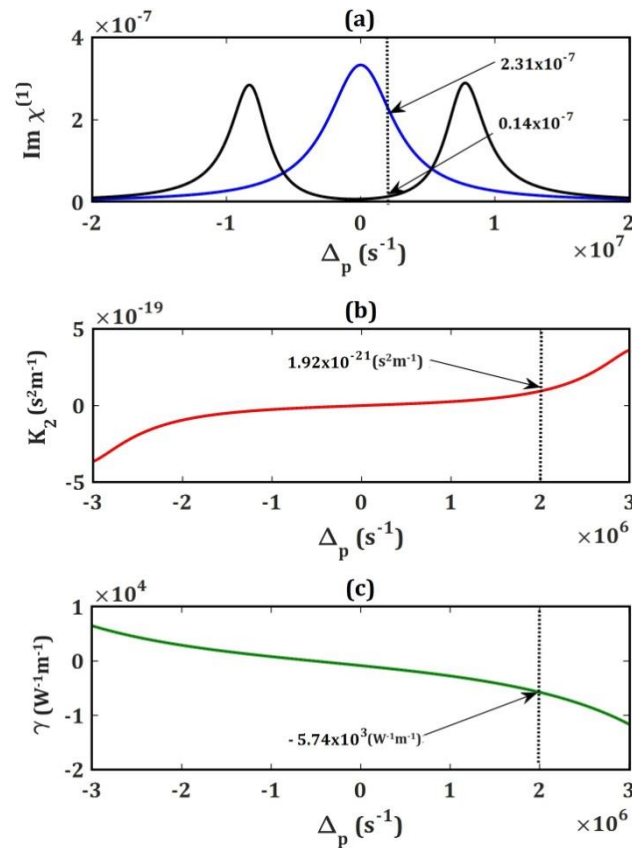


Figure 4: (a) Change in $\text{Im}\chi^{(1)}$ with probe detuning Δ_p (b) Alteration of K_2 with probe detuning Δ_p at 0.2×10^7 (c) Fluctuation of γ with probe detuning Δ_p at 0.2×10^7

Next we proceed to investigate the SC generation in the Rb vapour, for which a sec-hyperbolic pulse of the form $A = \sqrt{P_0} \text{sech}(t)$ of FWHM 1ns, with 100mW peak power is employed at probe wavelength 781nm. The obtained results are presented in figure 5 which depicts the density plots of spectral as well as temporal profiles throughout the propagation distance. From the

spectral profile presented in figure 5(a) it is evident that the initial pulse broadening, around 0.1 cm is purely dominated by self phase modulation (SPM) which indicates the production of symmetric oscillations in the pulse around the probe wavelength. The fact is also supported by the temporal pulse presented in figure 5(b), where the pulse is not broadened. With additional distance travelled, as a result of OWB induced by FWM, the pulse undergoes broadening on both sides of the probe wavelength. The same is evident from the temporal pulse towards the end of the cell distance where the pulse enhances little more in the negative time domain.

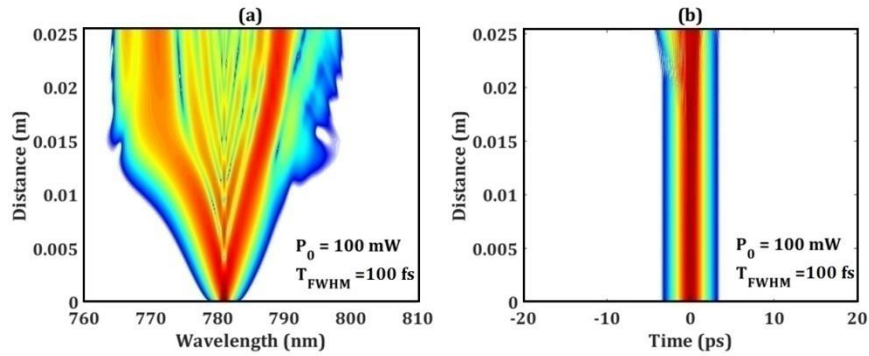


Figure 5: Density plot of the spectral evolution of a sech-pulse with pulse width 100fs and peak power of 100 mW, launched at 781 nm. (a) spectral and (b) temporal profile of the pulse.

(b) Density plot of the temporal evolution of 100fs input pulses at peak power of 100mW.

For more clarity we present the slices of SC profiles at input and output distances, as presented in figure 6. From the figure it is seen that the SC spectrum is composed of large oscillation dominated by SPM and OWB, and the spanning of the pulse is counted as 35 nm. The temporal pulse also shows both the features of SPM and OWB with pulse breaking in either side of the temporal pulse.

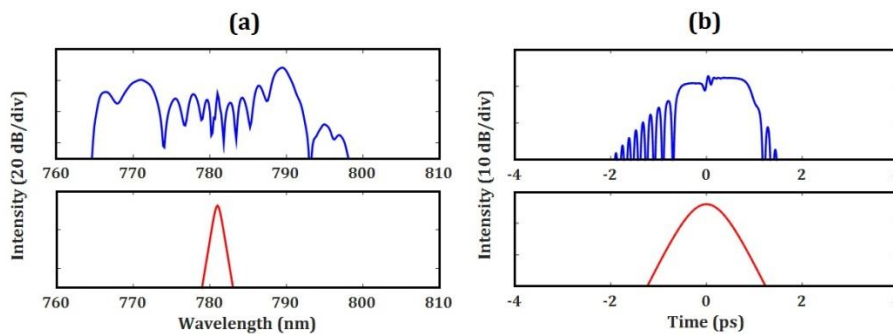


Figure 6: Input (bottom) and output (top) slices of the pulse, (a) Spectral and (b) temporal profiles.

4. Conclusion

We undertake a theoretical exploration of supercontinuum generation in a rubidium vapour cell operating under EIT conditions. Utilizing a weak probe pulse in conjunction with a strong control laser beam, we utilize a lambda-type excitation scheme. The rubidium vapour cell exhibits a substantial Kerr nonlinearity, reaching approximately $10^3 \text{ W}^{-1}\text{m}^{-1}$, and showcases low group velocity dispersion, approximately around $10^{-20} \text{ s}^2\text{m}^{-1}$, at a probe wavelength of 781 nm. These characteristics facilitate the generation of a 35 nm wide supercontinuum, distinguished by prominent oscillations stemming from self-phase modulation and optical wave breaking. Our findings hint at potential applications in nonlinear optical devices and spectroscopy.

5. Acknowledgement:

We would like to acknowledge the Infrastructural contribution of Shri M. Hoque, Chancellor of University of Science & Technology Meghalaya with heartfelt thanks.

References

1. R. H. Stolen, and C. Lin, 1978, Phys. Rev. A, 17, 1448.
2. Islam, M. N., Mollenauer, L. F., Stolen, R. H., Simpson, J. R., & Shang, H. T., (1987), Optics Letters, 12(8), 625-627
3. Lesvigne, C., Couderc, V., Tonello, A., Leproux, P., Barthélémy, A., Lacroix, S., ... & Georges, P. (2007). Optics letters, 32(15), 2173-2175
4. Zhang, L., Yan, Y., Yue, Y., Lin, Q., Painter, O., Beausoleil, R. G., & Willner, A. E., (2011), Optics express, 19(12), 11584-11590.
5. Coen, S., Chau, A. H. L., Leonhardt, R., Harvey, J. D., Knight, J. C., Wadsworth, W. J., & Russell, P. S. J., (2002), JOSA B, 19(4), 753-764
6. Demircan, A., & Bandelow, U., (2005), Optics Communications, 244(1-6), 181-185.
7. Demircan, A., & Bandelow, U., (2007), Applied Physics B, 86, 31-39.
8. Roy, S., Bhadra, S. K., & Agrawal, G. P., (2011), Current science, 321-342
9. Dudley, J. M., & Taylor, J. R. (Eds.), (2010), "Supercontinuum generation in optical fibers", Cambridge University Press.
10. Dudley, J. M., Genty, G., & Coen, S., (2006), Reviews of modern physics, 78(4), 1135
11. D. Budker, D. F. Kimball, and D. P. DeMille, (2004), "Atomic Physics: An Exploration through Problems and Solutions," Oxford University Press.
12. P. Russell, "Photonic Crystal Fibers," 2003, Science, vol. 299, no. 5605, pp. 358-362.
13. H. J. Metcalf and P. van der Straten, 1999, Springer-Verlag.
14. G. P. Agrawal, 2012, "Nonlinear Fiber Optics," Academic Press.
15. Zhu, C., Liu, Y., Xu, W., & Zhang, J., (2016), Optics Letters, 41(16), 3706-3709.
16. Jing, J., Wu, L., Wang, Y., & Zhang, J., (2019), Optics Express, 27(10), 13943-13953.
17. Li, Z., Bai, X., & Zhang, Y. (2020). Phys. Rev. A, 101(1), 013815.
18. Fleischhauer, M., Imamoglu, A., & Marangos, J. P., (2005), Reviews of Modern Physics, 77(2), 633-673.
19. Lukin, M. D., (2003), Reviews of Modern Physics, 75(2), 457-472.
20. Bajcsy, M., Zibrov, A. S., & Lukin, M. D., (2003), Nature, 426, 638-641.
21. Huang, G., Deng, L., & Payne, M. G., (2005), Phys. Rev. E, 72(1), 016617.
22. Han, Y., et al., (2021), Optics Express, 29(14), 21045-21055
23. Zhang, L., et al., (2022), Phys. Rev. A, 105(5), 053813
24. Xiao, M., et al., (2021), JOSA B, 38(9), 2685-2693
25. Chen, S., et al., (2023), Optics Letters, 48(2), 387-390
26. A J Olson, S. K. Mayer, (2008), Am. J. Phys. 77, 116-121.
27. Nath, M., Mukherjee, R., & Borgohain, N., (2023), Scientific Reports, 13(1), 7669.